



# Large-Area Smooth Conductive Films Enabled by Scalable Slot-Die Coating of $Ti_3C_2Tx$ MXene Aqueous Inks

## Journal Article

### Author(s):

Guo, Tiezhu; Zhou, Di; Gao, Min; Deng, Shungui; Jafarpour, Mohammad; Avaro, Jonathan; Neels, Antonia; [Hack, Erwin](#) ; [Wang, Jing](#) ; Heier, Jakob; Zhang, Chuanfang (John)

### Publication date:

2023-04-11

### Permanent link:

<https://doi.org/10.3929/ethz-b-000600986>

### Rights / license:

[Creative Commons Attribution 4.0 International](#)

### Originally published in:

Advanced Functional Materials 33(15), <https://doi.org/10.1002/adfm.202213183>

# Large-Area Smooth Conductive Films Enabled by Scalable Slot-Die Coating of $\text{Ti}_3\text{C}_2\text{T}_x$ MXene Aqueous Inks

Tiezhu Guo, Di Zhou, Min Gao, Shungui Deng, Mohammad Jafarpour, Jonathan Avaro, Antonia Neels, Erwin Hack, Jing Wang, Jakob Heier,\* and Chuanfang (John) Zhang\*

Large-area flexible transparent conductive electrodes (TCEs) featuring excellent optoelectronic properties (low sheet resistance,  $R_s$ , at high transparency,  $T$ ) are vital for integration in transparent wearable electronics (i.e., antennas, sensors, supercapacitors, etc.). Solution processing (i.e., printing and coating) of conductive inks yields highly uniform TCEs at low cost, holding great promise for commercially manufacturing of transparent electronics. However, to formulate such conductive inks as well as to realize continuous conductive films in the absence of percolation issue are quite challenging. Herein, the scalable slot-die coating of  $\text{Ti}_3\text{C}_2\text{T}_x$  MXene aqueous inks is reported for the first time to yield large-area uniform TCEs with outstanding optoelectronic performance, that is, average DC conductivity of  $13\,000 \pm 500 \text{ S cm}^{-1}$ . The conductive MXene nanosheets are forced to orientate horizontally as the inks are passing through the moving slot, leading to the rapid manufacturing of highly aligned MXene TCEs without notorious percolation problems. Moreover, through tuning the ink formulations, such conductive MXene films can be easily adjusted from transparent to opaque as required, demonstrating very low surface roughness and even mirror effects. These high-quality, slot-die-coated MXene TCEs also demonstrate excellent electrochemical charge storage properties when assembled into supercapacitors.

## 1. Introduction


The scalable printing/coating of nanomaterials from solution into highly conductive films is critical for diverse applications, including conventional electronics and transparent electronics, such as electromagnetic interference shielding,<sup>[1]</sup> antennas,<sup>[2]</sup> supercapacitors, touch screens,<sup>[3]</sup> or sensors,<sup>[4]</sup> to name just a few. Flexible transparent conductive electrodes (TCEs) display enormous potential for integration in next-generation wearable electronics.<sup>[5]</sup> In principle, coated nanomaterials should possess high intrinsic conductivity and in the case of TCEs show low sheet resistance ( $R_s$ ) at high transparency ( $T > 80\%$ ) without any percolation problems. Here, the percolation problem refers to a dramatic increase of  $R_s$  when the films thickness falls below the threshold, where continuous conductive pathways decrease, deviating from the bulk-like behavior at high transmittance.<sup>[6]</sup> It implies that TCEs

T. Guo, C. (John) Zhang  
College of Materials Science & Engineering  
Sichuan University  
Chengdu, Sichuan 610065, China  
E-mail: chuanfang.zhang@scu.edu.cn

T. Guo, S. Deng, M. Jafarpour, J. Heier  
Laboratory for Functional Polymers  
Empa

Swiss Federal Laboratories for Materials Science and Technology  
Überlandstrasse 129, CH-8600 Dübendorf, Switzerland  
E-mail: jakob.heier@empa.ch

T. Guo, D. Zhou  
Key Laboratory of Multifunctional Materials and Structures  
Ministry of Education, School of Electronic Science and Engineering  
Xi'an Jiaotong University  
Xi'an, Shaanxi 710049, China

 The ORCID identification number(s) for the author(s) of this article can be found under <https://doi.org/10.1002/adfm.202213183>.

© 2023 The Authors. Advanced Functional Materials published by Wiley-VCH GmbH. This is an open access article under the terms of the Creative Commons Attribution License, which permits use, distribution and reproduction in any medium, provided the original work is properly cited.

M. Gao, J. Wang  
Institute of Environmental Engineering  
ETH Zürich  
8093 Zürich, Switzerland

M. Gao, J. Wang  
Laboratory for Advanced Analytical Technologies  
Empa

Swiss Federal Laboratories for Materials Science and Technology  
Überlandstrasse 129, 8600 Dübendorf, Switzerland

S. Deng, M. Jafarpour  
Institute of Materials Science and Engineering  
Ecole Polytechnique Fédérale de Lausanne (EPFL)  
Station 12, CH-1015 Lausanne, Switzerland

J. Avaro  
Center for X-ray Analytics  
Empa

Swiss Federal Laboratories for Materials Science and Technology  
Lerchenfeldstrasse 5, CH-9014 St. Gallen, Switzerland

J. Avaro  
Biomimetic Membranes and Textile  
Empa

Swiss Federal Laboratories for Materials Science and Technology  
Lerchenfeldstrasse 5, CH-9014 St. Gallen, Switzerland

DOI: 10.1002/adfm.202213183

should have continuous conductive pathways at high  $T$ . For example, ultrathin films based on metal grids, Ag nanowires ( $\approx 50\,000\text{ S cm}^{-1}$ ),<sup>[7]</sup> single crystal graphite ( $\approx 20\,000\text{ S cm}^{-1}$ ),<sup>[8]</sup> Carbon nanotubes ( $\approx 20\,000\text{ S cm}^{-1}$ ),<sup>[9]</sup> PEDOT: PSS ( $4380\text{ S cm}^{-1}$ ),<sup>[10]</sup>  $\text{Ti}_3\text{C}_2\text{T}_x$  MXene ( $\approx 24\,000\text{ S cm}^{-1}$ ),<sup>[11]</sup> etc., are promising candidates for flexible TCEs. Despite the metal grids based TCEs display excellent optoelectronic properties, the feature sizes of high-precision and narrow wire-width were limited to complex manufacturing processes or sophisticated equipment. Moreover, the insulating islands between metallic conduits exhibit uneven electrical conductivity, thermal conductivity, and non-electrochemical energy storage performance,<sup>[12]</sup> inherently restricting its application. Ag nanowire-based TCEs also suffer from poor adhesion on flexible substrates.<sup>[13]</sup> On the other hand, solution processing of conductive materials into TCEs represent a facile and scalable strategy at low cost, however, the conductivity of most solution-processed TCEs is typically low, especially for 2D materials like graphene.<sup>[8]</sup> Moreover, the surface roughness of solution-processed TCEs is quite high, which further lowers down the transparency at a similar given thickness and thus compromises the thin film quality. In other words, developing conductive inks and suitable solution-processing strategies to yield TCEs at room temperature is of high necessity and urgent.

Decreasing the percolation threshold at high  $T$  is the key to the formation of continuous conductive pathways with less junctions.<sup>[6]</sup> For example, the highly aligned structures of metal micro-meshes decrease the percolation threshold.<sup>[13]</sup> 1D/2D hybrid materials have been investigated to overcome the nanowire junction problems, 2D flakes connected the insulating islands to enable uniform electrical conductivity.<sup>[12,14]</sup> MXenes, as an emerging family of 2D transition metal carbides, nitrides, or carbonitrides (general formula for  $\text{M}_{n+1}\text{X}_n\text{T}_x$  with  $n = 1-4$ ), possess metallic conductivity, hydrophilicity, high mechanical strength, etc.<sup>[15]</sup> In addition, due to the presence of abundant hydrophilic groups, as-synthesized MXenes allow the formation of colloidal stable additive-free inks at ease,<sup>[16]</sup> enabling the direct solution processing, such as printing and coating, into functional films/devices. These functional films and devices have demonstrated promising applications in supercapacitors,<sup>[17]</sup> batteries,<sup>[18]</sup> electromagnetic shielding,<sup>[19]</sup> sensors,<sup>[20]</sup> etc. Impressively, as the most widely studied MXene,  $\text{Ti}_3\text{C}_2\text{T}_x$  possesses the highest conductivity ( $\approx 24\,000\text{ S cm}^{-1}$ )<sup>[11]</sup> in all solution-processed 2D materials films reported so far, rendering  $\text{Ti}_3\text{C}_2\text{T}_x$  MXene as quite promising TCE material. It is worth

noting that flake size matters in realizing the high-performance TCEs;<sup>[21]</sup> small-sized  $\text{Ti}_3\text{C}_2\text{T}_x$  flakes ( $<1\ \mu\text{m}$ ) leads to the presence of abundant junctions and correspondingly dramatically increased  $R_s$  in the high transmittance region ( $>80\%$ ),<sup>[22]</sup> which significantly deviates from the ( $R_s$ ,  $T$ ) dataset fitting curves according to Equation 1,<sup>[23]</sup> known as the percolation problems.

$$T = \left( 1 + \frac{188.5 \sigma_{op}}{R_s \sigma_{DC}} \right)^{-2} \quad (1)$$

where  $\sigma_{op}$  is the optical conductivity,  $\sigma_{DC}$  is the DC conductivity, figure of merit ( $\text{FOM}_e$ ) is defined as the ratio of  $\sigma_{DC}/\sigma_{op}$  for evaluating optoelectronics performance. For example, Zhang et al.<sup>[23a]</sup> optimized the  $\text{Ti}_3\text{C}_2\text{T}_x$  flakes sizes to  $\approx 3.2\ \mu\text{m}$  from  $\approx 270\text{ nm}$ , spin-coated TCEs with an average conductivity up to  $7450\text{ S cm}^{-1}$ . However, the solution manufacturing methods such as spin coating,<sup>[22b,23a]</sup> spray coating,<sup>[24]</sup> dip coating,<sup>[22a,25]</sup> etc., are limited to coatings on small substrates and are utterly unsuitable for scalable production, limiting their development toward industrial manufacturing. Up to now, scalable solution printing/coating of TCEs without percolation issues is still challenging, especially for scalable solution printing/coating of large-area TCEs.

Slot-die coating is a very efficient method for scalable production of thin films with very low surface roughness, providing an ink of predominantly single/few-layer  $\text{Ti}_3\text{C}_2\text{T}_x$  flakes and proper process parameters. The ink can directly be coated on various rigid or flexible substrates such as glass, polyethylene terephthalate (PET), poly (ether sulfone), polydimethylsiloxane (PDMS).<sup>[26]</sup> Furthermore, benefits of slot-die coating include its pre-metered thickness control from several nanometers to micrometers, non-contact coating mechanism, and broad range of viscosities, from  $<1\text{ mPa s}$  to several thousand  $\text{Pa s}$ . Still, slot-die coating requires careful setting of processing parameters, most important coating speed and gap height, to guarantee defect-free coatings. A rough guidance can be given by the visco-capillary model that correlates ink properties and coating speed to the minimum wet film thickness required to form a stable wet film.<sup>[27]</sup> Only few works deal with slot-die coating of particle suspensions.<sup>[28]</sup> Worth mentioning are the simulations of “particle migration and alignment in slot coating flows of elongated particle suspensions”,<sup>[29]</sup> where it was found that particle orientation is influenced by the shear forces within the ink that is a strong function of processing parameters. For the selected values, in the film formation region, at the free surface particles align almost perfectly parallel to the substrate. Hence, the slot-die coating combined with high-quality MXene inks (predominantly single/few-layers flakes, large lateral sizes, narrow size distribution, and physical stability) hold great promise for fabricating high performance transparent and non-transparent films, especially for manufacturing large area TCEs.

In this work, we report on the uniform, scalable fabrication of  $\text{Ti}_3\text{C}_2\text{T}_x$  films ( $\approx 250\text{ cm}^2$ ) from transparent to non-transparent, based on direct slot-die coating of  $\text{Ti}_3\text{C}_2\text{T}_x$  inks at different concentrations.

The slot-die-induced shear force endows  $\text{Ti}_3\text{C}_2\text{T}_x$  flakes to assemble parallel to the substrate and form films with low surface roughness. The  $\text{Ti}_3\text{C}_2\text{T}_x$  films exhibit an average conductivity up to  $13\,000 \pm 500\text{ S cm}^{-1}$  on glass substrates for both

A. Neels  
Department of Chemistry  
University of Fribourg  
Chemin du Musée 9, CH-1700 Fribourg, Switzerland

A. Neels  
Center for X-ray Analytics  
Empa  
Swiss Federal Laboratories for Materials Science and Technology  
Überlandstrasse 129, CH-8600 Dübendorf, Switzerland

E. Hack  
Transport at Nanoscale Interfaces  
Empa  
Swiss Federal Laboratories for Materials Science and Technology  
Überlandstrasse 129, CH-8600 Dübendorf, Switzerland

opaque and transparent films. The MXene TCE demonstrates a high  $FOM_c$  and typical bulk-like behavior without notorious percolation problems. The optoelectronic performance of  $Ti_3C_2T_x$  TCEs can be easily controlled by adjusting the slot-die processing conditions, ink concentration, and substrates, etc. These  $Ti_3C_2T_x$  TCEs also exhibit excellent electrochemical charge storage properties for micro-supercapacitors. The strategy of scalable producing large-area MXene transparent films using slot-die technology is also general, holding a great potential in transparent energy storage or integrated electronics.

## 2. Results and Discussion

### 2.1. Synthesis and Characterization of $Ti_3C_2T_x$ Flakes

As shown in **Figure 1a**, in the stable operation regime, the solution continuously flows through the slot-die head, such that a stable meniscus forms between die and the substrate moving underneath at a fixed distance (gap height). The as-delaminated MXene flakes possess a smooth surface with an average lateral size of  $\approx 6 \mu\text{m}$  (the largest lateral size is up to  $13 \mu\text{m}$ ), as shown in the scanning electron microscope (SEM) image (**Figure 1b**) and the size histogram (**Figure 1c**), respectively. The delaminated flakes are of high quality and ultrathin, best evidenced by the absence of obvious pin-holes or apparent defects and the high transparency under the transmission electron microscope (TEM) electron beam (**Figure 1d**). To further examine the number of nanosheet layers per flake, atomic force microscopy (AFM)

(AFM) was conducted (**Figure 1e**). The corresponding height profiles along different lines suggest that the thickness of the flakes is  $\approx 1.7 \text{ nm}$  which is consistent with previous report.<sup>[30]</sup> These results demonstrate that a MXene dispersion enriched with single-layer  $Ti_3C_2T_x$  flakes was achieved. The dispersion was further subjected to high-speed cascade centrifugation and homogeneous mixing, leading to the formation of homogeneous MXene inks.

### 2.2. Analysis and Characterization of Transparent Films

By adjusting the inks concentration and slot-die processing parameters, large-area ( $\approx 250 \text{ cm}^2$ ), uniform, transparent  $Ti_3C_2T_x$  films were prepared on glass and flexible substrates (PET and PDMS), respectively, as shown in **Figure 2a,b** and **Figure S1** (Supporting Information). We used laser scribing to form various patterned transparent films for applications in electronics (i.e., antennas, sensors, supercapacitors, circuits, etc.), as shown in **Figure 2c**, demonstrating the advantages of scalable fabrication of TCEs. Stable coating conditions are detailed in the Supporting Information (**Figures S2 and S3**, Supporting Information). Interestingly, the rather large elastic component to the modulus (**Figure 2d**) does not affect coating stability. Foundation for high performing films are inks consisting of predominantly single/few-layer  $Ti_3C_2T_x$  flakes. The surface morphology of TCEs with similar transmittance ( $T = 72\text{--}74\%$ ) on different substrates is visualized by SEM and shown in **Figure S4** (Supporting Information). The cross-sectional focus-ion beam

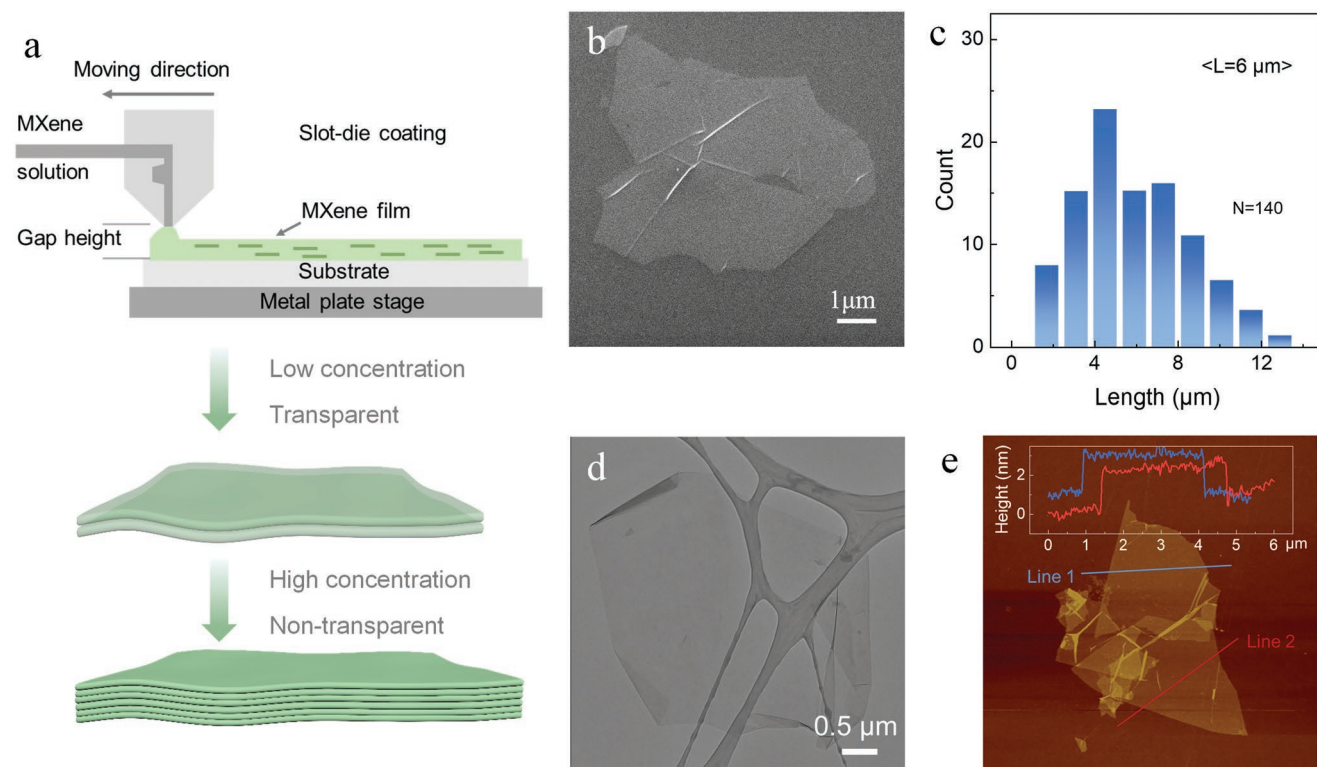


**Figure 1.** a) Schematic illustration of slot-die coating of smooth, conductive transparent, and non-transparent films. b,c) SEM image and  $Ti_3C_2T_x$  flake size histogram. d) TEM image of a  $Ti_3C_2T_x$  flake. e) AFM image of  $Ti_3C_2T_x$  flakes and height profiles of the different marked lines.



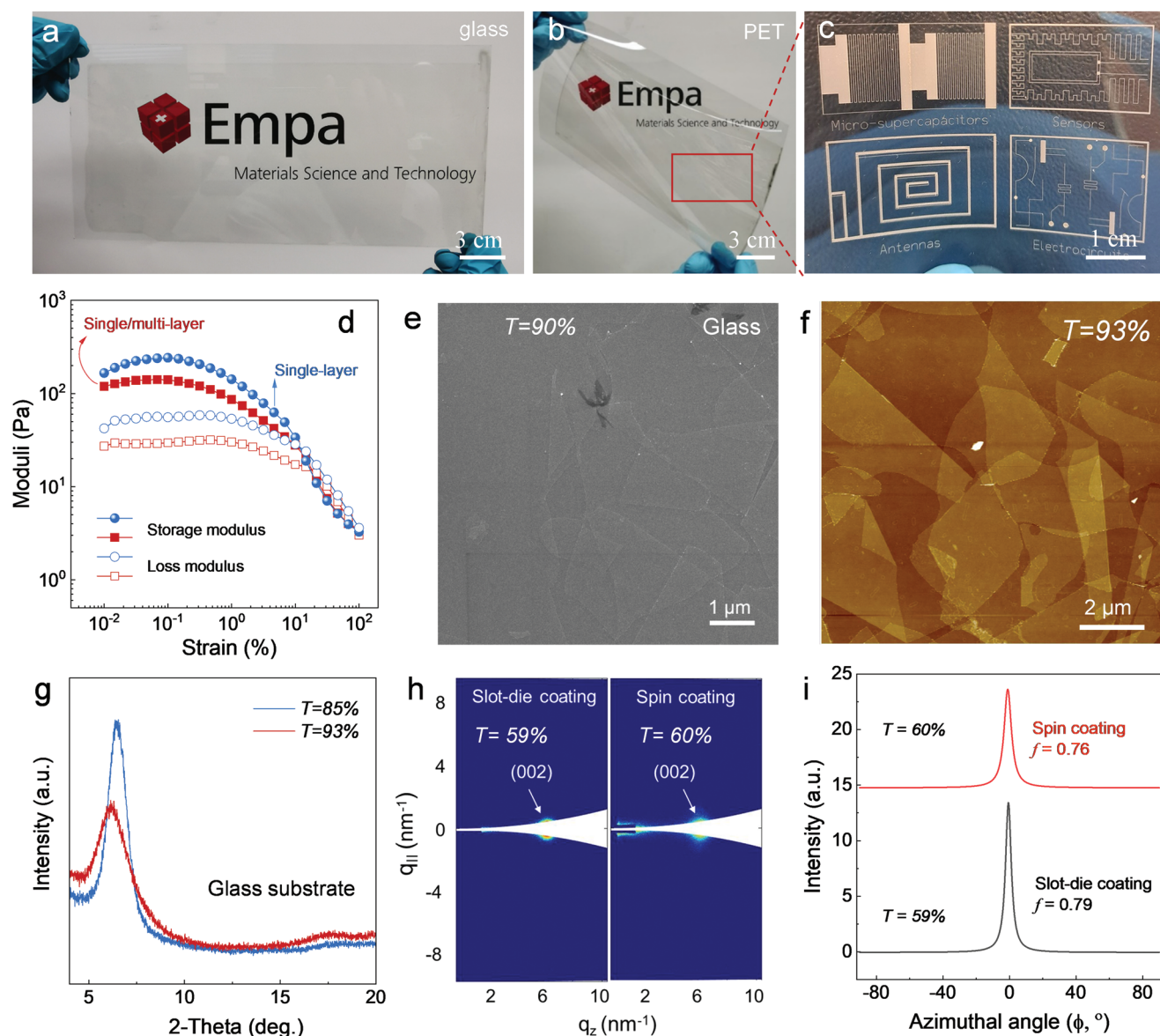


**Figure 2.** Characterizations of  $\text{Ti}_3\text{C}_2\text{T}_x$  TCEs. Digital photograph of  $\text{Ti}_3\text{C}_2\text{T}_x$  films on glass a) and PET b) substrates. c) Digital Photograph of integrated transparent electronics on large-area TCEs by laser scribing. d) Rheology of single-layer and single/multi-layer MXene inks at  $4 \text{ mL}^{-1}$ . e) Top-view SEM image of a MXene film on glass of  $T = 90\%$ . f) AFM image of  $T = 93\%$  TCEs. g) XRD patterns of TCEs with different transparency on glass. To contrast slot-die and spin-coated TCEs at similar transmittance ( $\approx T = 60\%$ ), GISAXS wedge plot showing the (002) peak over  $q_z$ . h, i) Lorentzian fit of the azimuthal profile for (002) peaks used to determine Herman's degree of orientation.

SEM (FIB-SEM) image showcases a smooth film thickness of  $\approx 11.5 \text{ nm}$  (Figure S5, Supporting Information). Notably, the surface topography of the substrate translates into the MXene film features:  $\text{Ti}_3\text{C}_2\text{T}_x$  flakes cover a glass substrate smoothly with connected flakes and without noticeable wrinkles. This is fundamentally distinct from films supported on the PET substrate that shows an intrinsic rough surface topography (Figure S6, Supporting Information). The hydrophilicity of various substrates does not change within 1 h after oxygen plasma pre-treatment, as detailed in Figure S7 (Supporting Information). The SEM surface topography (Figure 2e) showcases that the transparent film ( $T = 90\%$ ) displays a smooth surface with several micron-sized flakes continuously and closely covering the glass

substrate. We compared the surface topography of published works with our TCEs, and the lack of sharp contrast proves the advantages of the slot-die-coated film (Figure S8, Supporting Information). Furthermore, AFM confirmed that the uniform large-size  $\text{Ti}_3\text{C}_2\text{T}_x$  flakes continuously cover the glass substrate for the  $T = 93\%$  films (Figure 2f), which is the guarantee for low  $R_s$  at high  $T$ . The average surface roughness ( $R_a$ ) is  $\approx 0.93 \text{ nm}$ ; this value is significantly lower than roughness values reported for  $\text{Ti}_3\text{CNT}_x$  MXene TCEs ( $T = 80\% @ R_a = 2.7 \text{ nm}$ ) fabricated through spin-coating.<sup>[31]</sup> We attribute this to the fact that the slow coating speed is conducive to the formation of low-roughness films. The large lateral flake size should also contribute to the excellent surface smoothness. The  $R_s$  of different  $T$  such as

$T = 85\% @ R_a = 1.9 \text{ nm}$ ,  $T = 61\% @ R_a = 3.6 \text{ nm}$  is also shown in Figure S9 (Supporting Information).

The characteristic X-ray diffraction (XRD) peak of the  $\text{Ti}_3\text{C}_2\text{T}_x$  at  $\approx 6.2\text{--}6.5^\circ$  is shown in Figure 2g, indicating that the crystalline behavior of the high transmittance  $\text{Ti}_3\text{C}_2\text{T}_x$  films ( $T = 85\%$ ,  $T = 93\%$ ) is maintained, similar to opaque  $\text{Ti}_3\text{C}_2\text{T}_x$  films.<sup>[17a]</sup> A higher transmittance corresponds to the broadening of the (002) peak with reduced peak intensity, in good agreement with the literature.<sup>[22a]</sup> To examine the advantages of slot-die coating of MXene inks over spin coating method in enhancing the flakes alignment, the degree of orientation of  $\text{Ti}_3\text{C}_2\text{T}_x$  flakes was studied by performing grazing-incidence small-angle X-ray scattering (GISAXS) on two samples with similar transmittance ( $\approx T = 60\%$ ,  $\approx 23 \text{ nm}$ ). We compared the shape of the (002) reflection present at  $q_z \approx 6.2 \text{ nm}^{-1}$  (Figure 2h) and fitted its azimuthal profile with a Lorentzian curve (Figure 2i). The degree of orientation was calculated using Herman's orientation factor ( $f$ ) as previously used for MXene flakes in transmission mode.<sup>[32]</sup> The obtained  $f$  reveals that the slot-die-coated film possesses a slightly higher value (0.79) than the spin-coated film (0.76), indicating  $\text{Ti}_3\text{C}_2\text{T}_x$  flakes assemble into a more compact/aligned microarchitecture on glass under slot-die coating's shear force.

### 2.3. Analysis and Characterization of Opaque Films

We further investigated morphology and conductivity of slot-die-coated  $\text{Ti}_3\text{C}_2\text{T}_x$  films on various substrates. We prepared opaque films with low surface roughness and mirror effect with a high concentration  $\text{Ti}_3\text{C}_2\text{T}_x$  ink  $\approx 30 \text{ mg mL}^{-1}$ , as detailed in the Supporting Information. Figure 3a showcases photographic images of  $\text{Ti}_3\text{C}_2\text{T}_x$  films ( $\approx 250 \text{ cm}^2$ ) coated on glass and PET substrates, respectively. Interestingly,  $\text{Ti}_3\text{C}_2\text{T}_x$  films exhibit unique specular effects that are significant and clearly distinguished from the previously reported  $\text{Ti}_3\text{C}_2\text{T}_x$  films by slot-die coating<sup>[26]</sup> and blade coating<sup>[32]</sup> indicating low surface roughness with compact structures formed under strong shear forces. Sonicated small-sizes (average size of  $1 \mu\text{m}$ )  $\text{Ti}_3\text{C}_2\text{T}_x$  also demonstrates the mirror effect (Figure S10, Supporting Information), showing that the specular characteristic is independent of the  $\text{Ti}_3\text{C}_2\text{T}_x$  flakes sizes. The very high uniformity of the  $\text{Ti}_3\text{C}_2\text{T}_x$  ink and slot-die-coated films can also be inferred from its mirror like appearance. A heterogeneous or less uniform  $\text{Ti}_3\text{C}_2\text{T}_x$  ink (including oxidized inks) will severely diminish the specular effect or even make it disappear, as our experimental experience shows. In addition, the film produced by natural sedimentation (without shear force) such as drop-casting from uniform  $\text{Ti}_3\text{C}_2\text{T}_x$  ink also has no mirror effect. And, for the record, this is also the first report of MXene films with mirror effect. We imagine that one day we may build a flexible mirror that is foldable, attachable, and smart, for instance, we may combine this MXene foldable mirror with an antenna or radio frequency identification such that itself will fold-unfold automatically without manual operation. Moreover, MXene itself possesses excellent electromagnetic interference shielding/microwave absorption/antibacterial properties etc. Combining the MXene foldable mirror effect with these exotic properties renders more promising applications, such as in biotech and the like. Spectroscopic ellipsometry was used to determine the

thickness and optical parameters of  $\text{Ti}_3\text{C}_2\text{T}_x$  film on glass. For this  $200 \text{ nm}$  film, the reflection intensity was measured for several incidence angles. In addition, the reflectivity of bulk  $\text{Ti}_3\text{C}_2\text{T}_x$  was calculated from the optical parameters. These results are depicted in the Figure S11 (Supporting Information). Further, the optical parameters were modeled using a Drude term and a set of four additional Lorentz lines, in order to separate the intraband or free electron transitions (Drude) from the interband transitions.<sup>[33]</sup> The fit of the Drude term resulted in a scattering time of  $4.0 \text{ fs}$  and a resistivity of  $6.57 \times 10^{-5} \Omega \text{ cm}$ , corresponding to a conductivity of  $15\,000 \text{ S cm}^{-1}$ .

The surface topography (top-view) of  $\text{Ti}_3\text{C}_2\text{T}_x$  on glass and polyimide (PI) reveals a highly smooth surface, which is significantly smoother than films on PET, PDMS substrates (Figure 3b–e), and vacuum-assisted filtered films (Figure 3f). The wrinkle height of coated film on PET substrates is  $\approx 85 \text{ nm}$ , as shown in Figure S12 (Supporting Information). Previous work has demonstrated that unidirectional and periodic wrinkles in graphene oxide form upon drying the sample.<sup>[34]</sup> We believe that the wrinkles of  $\text{Ti}_3\text{C}_2\text{T}_x$  on PET depend on the roughness of the substrate, and then form after drying. According to AFM characterization, the average surface roughness ( $R_a$ ) of  $\text{Ti}_3\text{C}_2\text{T}_x$  film ( $\approx 300 \text{ nm}$ ) on glass is  $\approx 10.3 \text{ nm}$ , slightly lower than that of on PET ( $\approx 350 \text{ nm}$ ,  $R_a = 12.6 \text{ nm}$ , excluding wrinkle lines) and PI ( $\approx 340 \text{ nm}$ ,  $R_a = 12.0 \text{ nm}$ , excluding wrinkle lines) substrates. This result is consistent with the smoother and smaller roughness of the TCEs on the glass substrate. It is worth noting that the maximum height amplitude of the  $\text{Ti}_3\text{C}_2\text{T}_x$  film ( $\approx 300 \text{ nm}$ ) with specular effect and low roughness is only  $45 \text{ nm}$  on glass substrates. Low roughness, films assembled from aligned flakes showcase high electrical conductivity up to  $9837 \text{ S cm}^{-1}$  on glass without heat treatment. The conductivity remarkably increases to  $13\,337 \text{ S cm}^{-1}$  after post-heat treatment under Ar atmosphere at  $180^\circ \text{C}$  for 2 h, highlighting the necessity of heat treatment to achieve highly conductive MXene films.

The heat annealing-improved conductivity is also present in the flexible substrate PET, PI, and PDMS, as shown in Figure 3g and Table S1 (Supporting Information). Note that the heat treatment of  $\text{Ti}_3\text{C}_2\text{T}_x$  films is carried out at  $110^\circ \text{C}$  for 2 h for PET and PDMS substrates to stay within a tolerable temperature range. Heating of the PI and glass substrates is executed at  $180^\circ \text{C}$  for 2 h. Obviously, the annealing temperature plays a major role, the electrical conductivity of  $\text{Ti}_3\text{C}_2\text{T}_x$  films on glass and PI substrates increased substantially following heat treatment compared to that of PET and PDMS.

The conductivity improvement can be fairly attributed to the removal of water molecules between  $\text{Ti}_3\text{C}_2\text{T}_x$  flakes upon heat annealing, which results in much decreased interlayer spacing and facilitates the electron hopping among different layers.<sup>[32]</sup> On the other hand, according to Shao et al.,<sup>[35]</sup> the maximum weight loss of MXene because of removal of water between  $\text{Ti}_3\text{C}_2\text{T}_x$  interlayers as measured by temperature-programmed desorption occurs already at  $120^\circ \text{C}$ . As a consequence, the low-roughness  $\text{Ti}_3\text{C}_2\text{T}_x$  films on glass exhibits excellent electrical conductivity after being thoroughly dried. Also the nature of the substrate influences the interlayer spacing, the XRD patterns showcase that the (002) peaks of  $\text{Ti}_3\text{C}_2\text{T}_x$  (Figure 2h) are observed at  $7.4^\circ$  (glass),  $6.9^\circ$  (PI),  $6.9^\circ$



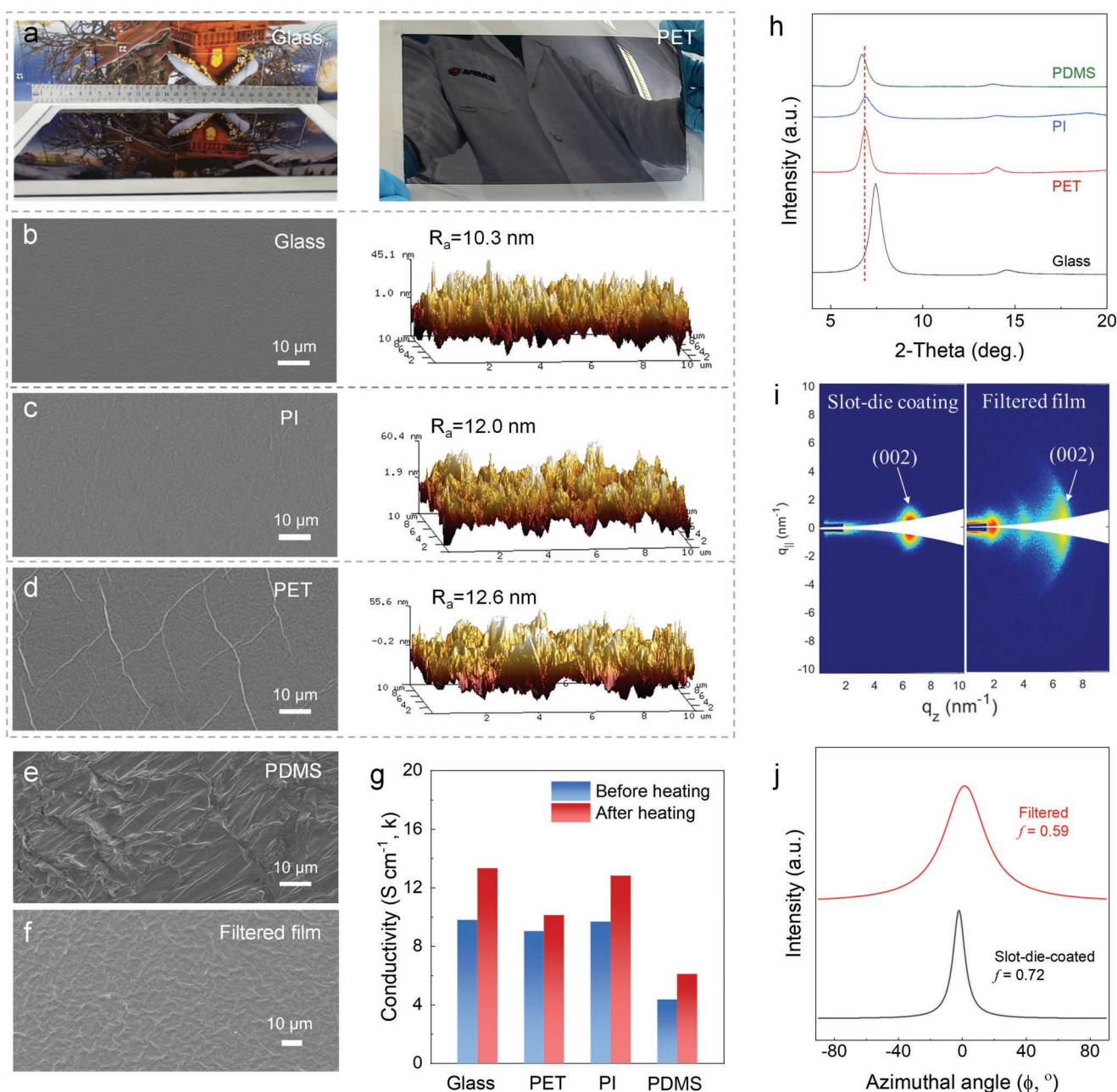


**Figure 3.** Characterizations of  $\text{Ti}_3\text{C}_2\text{T}_x$  opaque films. a) Digital photograph of  $\text{Ti}_3\text{C}_2\text{T}_x$  films on glass and PET substrates, showing the mirror effect indicative of low surface roughness. b–d) Top-view SEM and AFM images of opaque films supported on glass, PET, PI substrates. SEM images of e) MXene opaque film supported on PDMS and f) filtrated freestanding MXene film. Conductivity g) and XRD patterns h) of  $\text{Ti}_3\text{C}_2\text{T}_x$  on different substrates. To contrast slot-die-coated and filtered films, i) GISAXS detector images showing the (002) peak over  $q_z$  (h). j) Lorentzian fit of azimuthal profile for (002) peaks used to determine Herman's degree of orientation.

(PET),  $6.7^\circ$  (PDMS), corresponding to a  $c$  lattice parameter of 24.0, 25.7, 25.7, and 26.5 Å, respectively. Furthermore, slot-die-coated film possesses a much higher degree of orientation value ( $\approx 300$  nm,  $f = 0.72$ ) than filtered films ( $\approx 1$  μm,  $f = 0.59$ ), as shown in Figure 2i,h. In this case, the non-transparent films thickness is much larger than transparent films. The much increased orientation degree fully suggests the advantages brought by the slot-die coating technique in forcing the flakes to align in order.

The chemical composition and structure of transparent and non-transparent  $\text{Ti}_3\text{C}_2\text{T}_x$  films were investigated by Raman spectroscopy (Figure 4a) and X-ray photoelectron spectroscopy (XPS, Figure 4b). As shown in previous studies, the Raman fingerprint of  $\text{Ti}_3\text{C}_2\text{T}_x$  films appears between 100 and 800  $\text{cm}^{-1}$ .<sup>[36]</sup> The transparent and opaque films showed almost identical high-resolution XPS spectra in the Ti 2p region, indicating no obvious oxidation was observed from transparent films for at least 1 week (when stored in a glove box). The peaks at

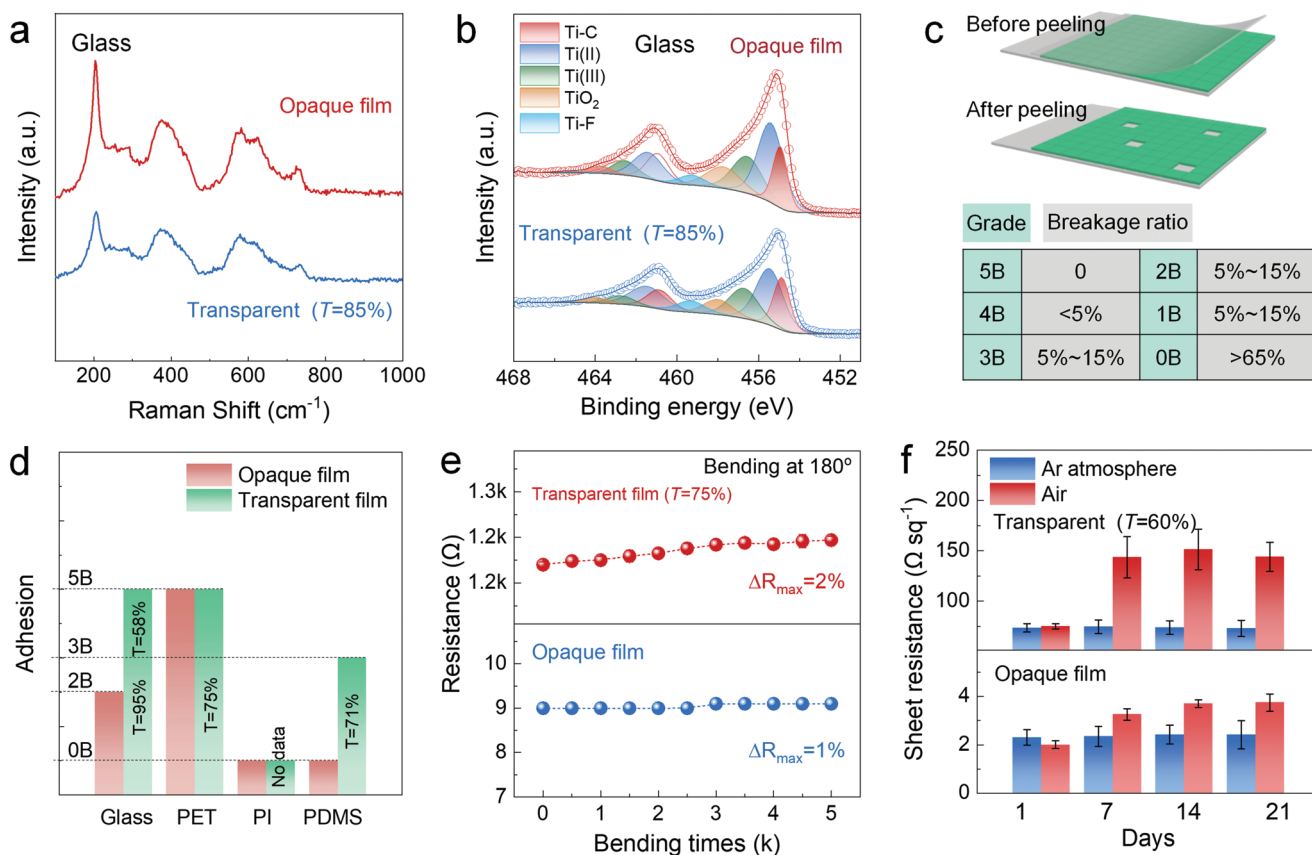


**Figure 4.** Comparison of transparent and opaque films. a) Raman spectra of slot-die-coated transparent and non-transparent films on glass. b) XPS spectra of slot-die-coated transparent and non-transparent films on glass showing binding energy values associated with Ti 2p. c) Schematic diagram of adhesion characterization grades for coated films according to ASTM D3359. 5B means that the coated film is intact after repeated tearing of the tape. 4B, 3B, 2B, 1B, and 0B represent exfoliated areas <5%, 5–15%, 15–35%, 35–65%, and >65%, respectively. d) Adhesion on different substrates, the thicknesses of Ti<sub>3</sub>C<sub>2</sub>T<sub>x</sub> on glass, PET, PI, and PDMS are ≈300, ≈350, ≈340, and ≈500 nm, respectively. e) Resistance of the coated film on PET substrate with different thickness (≈350 and ≈11 nm/T = 75%) as a function of bending times at 180°. f) R<sub>s</sub> of opaque (≈300 nm) and transparent films (T = 60%) on glass substrate as a function of time under ambient conditions and Ar atmosphere.

455.0, 455.8, 457.1, 458.5, and 459.4 eV represent Ti–C bonds, Ti<sup>2+</sup>, Ti<sup>3+</sup>, TiO<sub>2</sub>, and TiO<sub>2-x</sub>F<sub>x</sub>, respectively.<sup>[37]</sup> Note that in fresh MXene ≈5% TiO<sub>2</sub> or less can be detected, which is consistent with published reports.<sup>[37,38]</sup>

Since the adhesion of coated films to the substrate is of significance in practical applications, we further investigated the adhesion strength of transparent and opaque films on different substrates according to the American Society for Testing and Materials (ASTM) D3359 for coating adhesion. The adhesion grades are defined from low to high as 0B, 1B, 2B, 3B, 4B, 5B, respectively. While 5B means that the coated film is intact after repeated tearing of the tape, 0B suggests >65% of the area has been torn off (Figure 4c). The grade 5B of transparent Ti<sub>3</sub>C<sub>2</sub>T<sub>x</sub> films on PET (T = 75%) and glass substrates (T = 58–95%) suggest that as-slot-die-coated ultrathin films strongly adhere to the substrates. In sharp contrast, the Ti<sub>3</sub>C<sub>2</sub>T<sub>x</sub> opaque film on PI (≈340 nm) and PDMS (≈500 nm) substrate showcase quite low adhesion (0B), as MXene film was entirely peeled off (Figure 4d). We expect that Ti<sub>3</sub>C<sub>2</sub>T<sub>x</sub> films with high adhesion strength can maintain a small resistance change rate (ΔR%) or remain unchanged during repeated deformation, the latter is very important criteria in flexible electronics. Indeed, the

slot-die-coated film on PET substrate exhibits excellent flexibility and stable resistance after repeated bending cycles. For instance, the TCEs (T = 75%) demonstrated a ΔR% of only 2% after 5000 bending cycles at 180°. Notably, the resistance change is substantially lower than that of Ti<sub>3</sub>C<sub>2</sub>T<sub>x</sub> TCEs reported previously on PET substrate (increasing 20%, 1000 cycles).<sup>[39]</sup> No resistance change is detected from the opaque film (≈300 nm) after bending at 180° for 2500 cycles, and ΔR% is only 1% after 5000 cycles (Figure 4e), which is similar to the blade-coated Ti<sub>3</sub>C<sub>2</sub>T<sub>x</sub> film from 10 μm flakes.<sup>[32]</sup> The results indicate that slot-die-coated films possess superior deformation resistance thanks to the synergistic effect of excellent adhesion on PET and the compact, aligned structure of Ti<sub>3</sub>C<sub>2</sub>T<sub>x</sub> flakes under shear force. These slot-die-coated transparent (≈T = 60%) and opaque films are quite stable when storing in Ar atmosphere, best evidenced by the almost unchanged R<sub>s</sub> over a period of 21 days. However, the resistance increases considerably after 7 days storage in ambient conditions and remain then at a constant level (Figure 4f). We can draw two conclusions; first, moisture greatly influences the R<sub>s</sub> of films when exposed to ambient atmosphere. The other is that for opaque and low transparent films (T ≤ 60%), humidity factors showcase a more significant

effect on the  $R_s$  than oxidation in the air within 21 days, similar to the values reported previously.<sup>[22b]</sup>

## 2.4. Optoelectronic Properties of the Transparent Ti<sub>3</sub>C<sub>2</sub>T<sub>x</sub> Films

The UV-vis spectra of Ti<sub>3</sub>C<sub>2</sub>T<sub>x</sub> films with different thicknesses on glass and PET are shown in Figure 5a,b and Figure S13 (Supporting Information). The transmittance at 550 nm from

5 samples' average values is defined as the films' transmittance (Figure S14, Supporting Information), and the characteristic peak narrows down with the increase of film thickness. The relationship between the transmittance ( $T$ ) and sheet resistance ( $R_s$ ) of Ti<sub>3</sub>C<sub>2</sub>T<sub>x</sub> TCEs on different substrates, and fitted transmittance as a function of  $R_s$  according to Equation 1, is shown in Figure 5c. The  $R_s$  value of the MXene TCEs on glass reaches 498  $\Omega \text{ sq}^{-1}$  at  $T = 94.5\%$ , 192  $\Omega \text{ sq}^{-1}$  at  $T = 89\%$ , and 91  $\Omega \text{ sq}^{-1}$  at  $T = 78\%$ , substantially lower than that of other

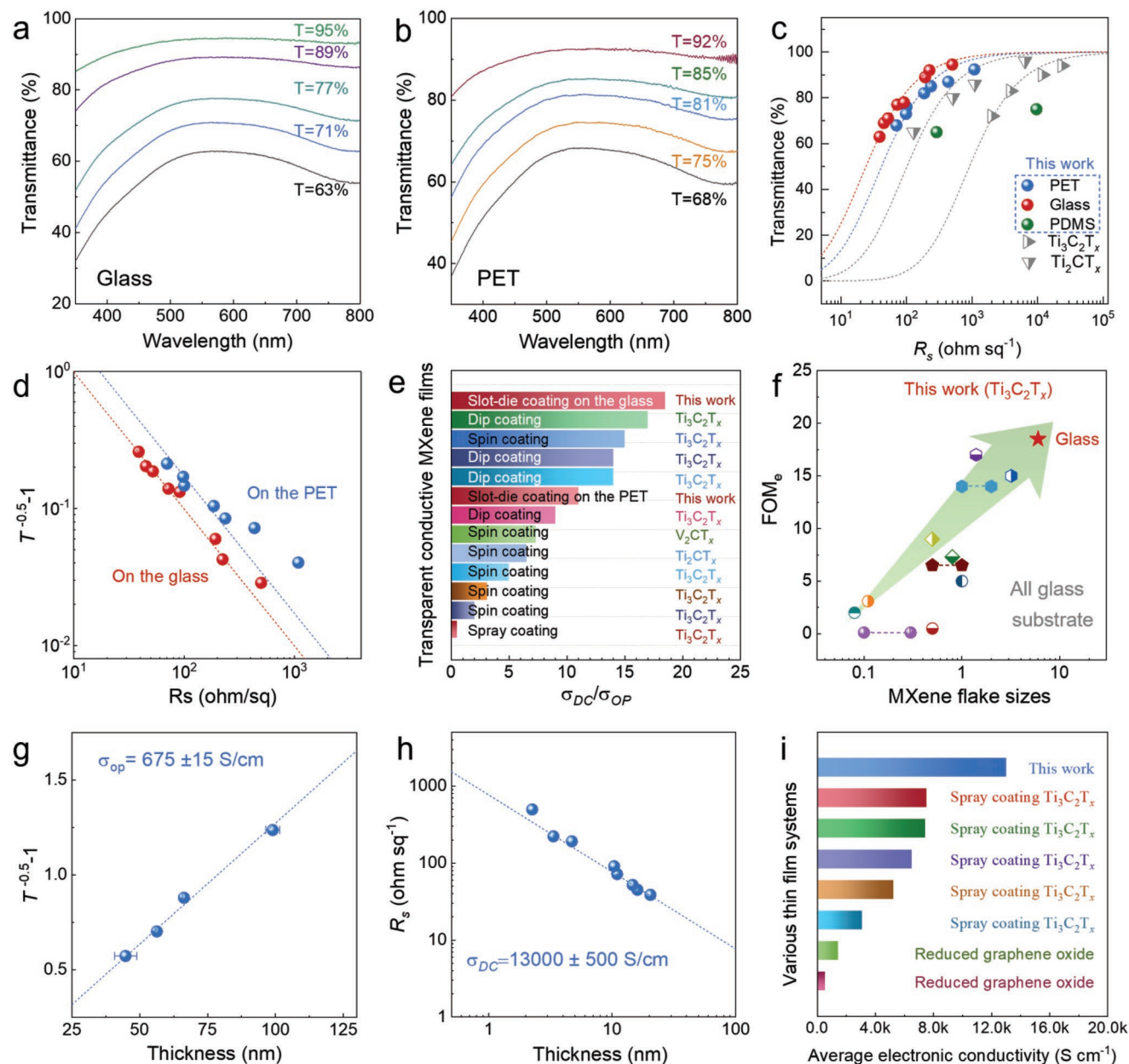


**Figure 5.** Optoelectronic properties of Ti<sub>3</sub>C<sub>2</sub>T<sub>x</sub> TCEs. UV-vis spectra of various transparent films supported on a) glass and b) PET. c) The relationship between  $T$  with  $R_s$ . Also included are fitting curves and  $(T, R_s)$  from other pieces of literature; detailed values are presented in Table S2 (Supporting Information). d)  $T^{-0.5-1}$  as a function of  $R_s$  to evaluate the bulk-like conductivity. e) To contrast the  $\sigma_{DC}/\sigma_{OP}$  (FOM<sub>e</sub>) with various transparent conductive MXene TCEs, detailed values are presented in Table S2 (Supporting Information). f) Relationship between FOM<sub>e</sub> and MXene flake sizes. g)  $T^{-0.5-1}$  as a function of the thickness ( $t$ , >20 nm), to obtain the optical conductivity ( $\sigma_{op}$ ) of Ti<sub>3</sub>C<sub>2</sub>T<sub>x</sub> TCEs. h)  $R_s$  as a function of  $t$  to gain the average DC conductivity ( $\sigma_{DC}$ ) of Ti<sub>3</sub>C<sub>2</sub>T<sub>x</sub> TCEs. i) Comparison of the average DC conductivity of various TCEs, detailed values are presented in Table S3 (Supporting Information).



published  $\text{Ti}_3\text{C}_2\text{T}_x$  TCEs in a similar transmittance range. For example, values are reported for spin-coating  $\text{Ti}_3\text{C}_2\text{T}_x$  ( $1\ 031\ \Omega\ \text{sq}^{-1}$  at  $T = 94\%$ )<sup>[23a]</sup> and dip-coating  $\text{Ti}_3\text{C}_2\text{T}_x$  ( $4300\ \Omega\ \text{sq}^{-1}$  at  $T = 94\%$ )<sup>[22a]</sup>. More important, at  $T > 80\%$ , the  $R_s$  still follows the fitting curve closely without obvious percolation problems. This is due to the fact that our ink contains uniform large-size flakes, without nanoscale small-size flakes as shown in Figure 2f. The  $R_s$  of  $\text{Ti}_3\text{C}_2\text{T}_x$  TCEs coated on PET substrate is slightly higher ( $1083\ \Omega\ \text{sq}^{-1}$  at  $T = 92.4\%$  and  $434\ \Omega\ \text{sq}^{-1}$  at  $87\%$ ), the  $(T, R_s)$  dataset significantly deviates from the fitting curve at  $T > 85\%$ , indicating the presence of percolation problems, which should be avoided. For coated TCEs on foldable PDMS substrates,  $R_s$  increases already dramatically at  $T > 60\%$ , with  $R_s$  values up to  $287\ \Omega\ \text{sq}^{-1}$  at  $T = 65\%$  and  $9600\ \Omega\ \text{sq}^{-1}$  at  $75\%$ . The considerable higher  $R_s$  at similar  $T$  than that of PET and glass substrates may be attributed to the abundant wrinkles and cracks caused by deformation (Figure S15, Supporting Information) and insufficient removal of water at  $110\ ^\circ\text{C}$ . The averaged (from fitting) and the maximum  $\text{FOM}_e$  of TCEs films on glass reaches 18.5 and 20.5, respectively (Table S2, Supporting Information). The  $R_s$  of TCEs on glass substrate is independent of thickness, suggesting that the as slot-die-coated film exhibits a typical bulk-like conductivity throughout the entire region, but not on flexible substrates such as PET and PDMS. The well-fitted data point in the  $T^{-0.5}$ -1 versus  $R_s$  curve further proves the absence of percolation problems. However, this bulk-like conductivity behavior is absent in films supported on PET, as evidenced by the deviation from the fitted curves in the high transparency region in Figure 5c,d. Such conductive MXene transparent films indeed outperform the rest solution-processed films in terms of  $\text{FOM}_e$  (Figure 5e). We believe the optoelectronic properties, in particular, this important metrics  $\text{FOM}_e$  can be further substantially improved by simply synthesizing larger-size MXene flakes, as the  $\text{FOM}_e$  generally increases with the enlargement of flake size (Figure 5f).

In order to obtain the conductivity of films with different transmittance, the thickness of homogeneous translucent film supported on glass was measured by contact profilometry. The optical conductivity,  $\sigma_{\text{op}}$  was obtained based on the Equation 2, we obtain the optical conductivity,  $\sigma_{\text{op}}$ .

$$T = (1 + 188.5\sigma_{\text{op}}t)^{-2} \quad (2)$$

where  $T$  is the film transmittance,  $t$  is the film thickness, after rearrangement,

$$T^{-0.5} - 1 = 188.5\sigma_{\text{op}}t \quad (3)$$

Linear fitting  $T^{-0.5}$  as a function of  $t$  yields a slope of  $188.5\sigma_{\text{op}}$ . As such, the  $\sigma_{\text{op}}$  for  $\text{Ti}_3\text{C}_2\text{T}_x$  TCEs on glass reaches  $675 \pm 15\ \text{S cm}^{-1}$  (Figure 5g), based on which the thickness for highly transparent films can be accurately calculated, as shown in Figure S16a (Supporting Information). With all  $R_s$  and thickness information, the DC conductivity of all films can be obtained based on Equation (3), ranging from 8906 to  $13\ 870\ \text{S cm}^{-1}$  (Figure S16b, Supporting Information), almost linear fitting of  $R_s$  versus  $t$  also suggests the bulk-like behavior, with the averaged conductivity of  $13\ 000 \pm 500\ \text{S cm}^{-1}$

(Figure 5h), the value from the fitting of all data in Figure 5h according to Equation 4.

$$R_s = \frac{1}{\sigma_{\text{DC}}t} \quad (4)$$

Notably, this value is significantly superior to previously reported  $\text{Ti}_3\text{C}_2\text{T}_x$  TCEs ( $7530\ \text{S cm}^{-1}$ ,<sup>[25]</sup>  $7450\ \text{S cm}^{-1}$ ,<sup>[23a]</sup> etc.) and reduced graphene oxide films ( $1425\ \text{S cm}^{-1}$ ,<sup>[40]</sup>  $550\ \text{S cm}^{-1}$ ,<sup>[41]</sup>), as shown in Figure 5i. (Table S3, Supporting Information). We believe that the excellent conductivity and outstanding optoelectronic properties of slot-die-coated large-area  $\text{Ti}_3\text{C}_2\text{T}_x$  TCEs are a consequence of the following two factors: i) Compared with conventional  $\text{Ti}_3\text{C}_2\text{T}_x$  TCEs made from flake sizes  $< 3\ \mu\text{m}$ , our  $\text{Ti}_3\text{C}_2\text{T}_x$  TCEs from large-sizes flakes showcases fewer interflake junctions (small interflake resistance). ii) The  $\text{Ti}_3\text{C}_2\text{T}_x$  TCEs are fabricated by slot-die coating, shear forces during deposition support a compact parallel arrangement on glass, facilitating electron migration.

## 2.5. Electrochemical Performance of $\text{Ti}_3\text{C}_2\text{T}_x$ Films

The excellent optoelectronic properties of slot-die-coated  $\text{Ti}_3\text{C}_2\text{T}_x$  TCEs imply that interconnected flakes can be employed as both transparent current collectors to efficiently conduct electrons and energy storage electrode materials to store ions/charge. As such, transparent all-MXene microsupercapacitors (MSC, interdigitated finger gap  $\approx 260\ \mu\text{m}$ ) were fabricated through laser scribing. The normalized cyclic voltammograms (CVs) of transparent MSC with different transmittance were studied from 10 to  $2000\ \text{mV s}^{-1}$ , as shown in Figure 6a and Figure S17a (Supporting Information). The transparent MSC with  $T = 70\%$  showcases a quasi-rectangular shape below  $200\ \text{mV s}^{-1}$  and spindle at  $2000\ \text{mV s}^{-1}$ , suggesting the capacitive charge-storage behavior and excellent rate response (maintaining 40% of initial capacitance at  $20\ \text{mV s}^{-1}$ ). This is further verified by the symmetrical triangular shape of galvanostatic charge-discharge (GCD) curves in Figure 6b. Such a capacitive charge storage behavior is also observed in the  $T = 60\%$  MSC (Figure S17b, Supporting Information).

These areal capacitances were calculated from CVs and GCD curves, respectively, suggesting similar values (Figure 6c; Figure S17c, Supporting Information). At  $T = 70\%$  and  $60\%$ , MSCs exhibit  $254$  and  $427\ \mu\text{F cm}^{-2}$  at  $20\ \text{mV s}^{-1}$ , respectively, this value is distinctly better than that of graphene-based MSC ( $T = 67\%$  @  $12.4\ \mu\text{F cm}^{-2}$ ,<sup>[42]</sup>  $T = 60\%$  @  $5.8\ \mu\text{F cm}^{-2}$ ,<sup>[43]</sup>) and published  $\text{Ti}_3\text{C}_2\text{T}_x$  MSC ( $T = 73\%$  @  $192\ \mu\text{F cm}^{-2}$ ,  $T = 38\%$  @  $283\ \mu\text{F cm}^{-2}$ ).<sup>[22a]</sup> In addition, we fitted the areal capacitance at different scan rates based on Equation 5.<sup>[23b]</sup>

$$C = C_A \left[ 1 - \frac{\nu\tau}{V} \left( 1 - e^{-\frac{\nu}{V}} \right) \right] \quad (5)$$

where  $C_A$  is the intrinsic rate-independent areal capacitance (no electronic or/and ionic transport limitations during charge-discharge),  $\tau = R_{\text{ESR}} C$  is the time-constant,  $\nu$  is the scan rate,  $\Delta V$  is the voltage window ( $0.6\ \text{V}$ ). Interestingly, the measured data are well distributed around the fitting lines. Figure 6d

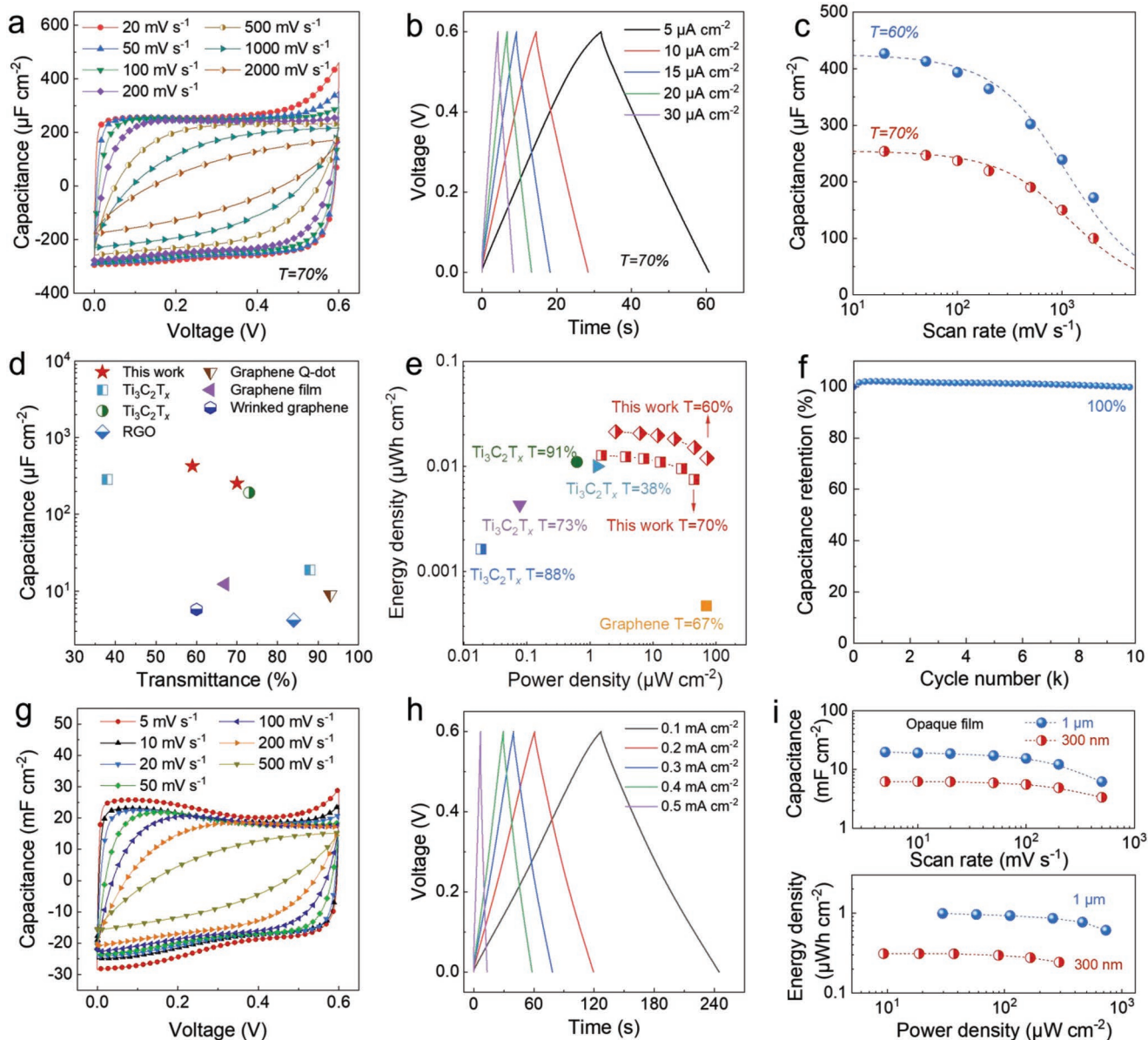


**Figure 6.** Electrochemical characterization of  $\text{Ti}_3\text{C}_2\text{T}_x$  symmetric MSCs. a) Normalized CV curves at various scan rates of  $T = 70\%$ . b) GCD curves at different current densities of  $T = 70\%$ . c) Measured areal capacitance obtained from CV curves, the dashed lines represent the capacitance fitting value according to Equation 5. d) Areal capacitance versus transmittance, and compared with other transparent supercapacitors. e) Ragone plots of MSCs with different transparencies, and comparison to other transparent supercapacitors, detailed values are presented in Table S4 (Supporting Information). f) Long-term cycling of transparent MSC ( $T = 70\%$ ). g, h) Normalized CV and GCD curves at various scan rates of opaque films with  $1 \mu\text{m}$ . i) Measured areal capacitance obtained from CV curves and Ragone plots.

showcases the areal capacitance of our transparent MSC and compares it with other reported similar works. Furthermore, the Ragone plot (energy density versus power density) summarizes this work and other reported previously transparent MSCs. The energy density of  $T = 70\%$  MSCs reaches  $0.0127 \mu\text{Wh cm}^{-2}$  at power density of  $1.524 \mu\text{W cm}^{-2}$ , which is superior to other  $\text{Ti}_3\text{C}_2\text{T}_x$  MSCs, that is,  $T = 73\% @ 0.0043 \mu\text{Wh cm}^{-2}$ ,<sup>[22c]</sup>  $T = 38\% @ 0.01 \mu\text{Wh cm}^{-2}$ <sup>[22a]</sup> (Figure 6e). The transparent  $\text{Ti}_3\text{C}_2\text{T}_x$  MSC ( $T = 70\%$ ) also exhibits outstanding cycling properties, retaining  $\approx 100\%$  of the initial capacitance after 9800 cycles (Figure 6f). These impressive electrochemical charge

storage performances indicate the promising application of transparent  $\text{Ti}_3\text{C}_2\text{T}_x$  MSC for next-generation transparent integrated electronics.

Besides the transparent TCEs for MSCs, we also evaluated the charge storage properties of MSCs based on slot-die-coated MXene films with  $1 \mu\text{m}$  and  $300 \text{nm}$  in thickness, respectively. Figure 6g, h and Figure S18 (Supporting Information) showcase the normalized CVs and GCD curves of laser-scribed MSCs. Interestingly, the CV curves turn into quite resistive as the scan rate goes beyond  $500 \text{mV s}^{-1}$ , indicating inferior rate performance compared to that of  $T = 70\%$  MSC. This is understandable,

as the highly compact and highly aligned flakes intrinsically impede the ion diffusion kinetics inside the thick films, unlike the ultrathin films whose top surface is utilized for charge storage. Figure 6i summarizes the areal capacitance and Ragone plot with different thicknesses. The areal capacitance of  $t = 1 \mu\text{m}$  MSC was calculated from CVs curves, exhibiting  $19.8 \text{ mF cm}^{-2}$  at  $5 \text{ mV s}^{-1}$ , and energy density of  $0.99 \mu\text{Wh cm}^{-2}$  at a power density of  $29.7 \mu\text{W cm}^{-2}$ , other detailed values are presented in Table S4 (Supporting Information). For the application of opaque films, volumetric specific capacitance is a more important parameter than areal specific capacitance. Thus, we calculated volumetric specific capacitance to be  $198 \text{ F cm}^{-3}$  at  $5 \text{ mV s}^{-1}$  for a  $\approx 1 \mu\text{m}$  thin film according to  $C_{\text{area}}/t = C_{\text{volume}}$ . To make a fair comparison, it is best and ideal to compare the performance of devices prepared with similar techniques. Here, we compare the volumetric specific capacitance of pure  $\text{Ti}_3\text{C}_2\text{T}_x$ -based MSCs prepared by spray-coating, which is  $212 \text{ F cm}^{-3}$  (lateral dimensions of  $3\text{--}6 \mu\text{m}$ ) and  $230 \text{ F cm}^{-3}$  (lateral dimensions of  $\approx 1 \mu\text{m}$ ) at  $20 \text{ mV s}^{-1}$ , respectively.<sup>[44]</sup> However, such a technique is easy to operate large-scale production.

### 3. Conclusion

To conclude, we demonstrate the scalable slot-die coating of MXene inks with optimized ink rheology to produce large-area ( $\approx 250 \text{ cm}^2$ ), uniform and highly conductive films with very low surface roughness at room temperature. Ultrathin films with excellent optoelectronic properties can be achieved at ease by adjusting slot-die conditions, ink concentration, and substrates. Importantly, the slot-die-coated films consist of interconnected, highly aligned MXene nanosheets, the latter forms compact and conductive paths such that the notorious percolation problem is beaten. Consequently, DC conductivity up to  $13\,000 \pm 500 \text{ S cm}^{-1}$  is achieved in the highly transparent films with excellent adhesion on PET and glass substrates, while poor adhesion on PDMS. This gives us a large flexibility to find specific applications with personal requirements on conductivity and/or transparency or adhesion. Such a slot-die coating of MXene inks strategy is also compatible with the laser scribing technique to produce transparent electronics such as transparent supercapacitors with superior capacitance, rate performance, and energy density, etc. The combination of slot-die coating of MXene inks with direct laser scribing technology also holds a great promise for rapid production of large-area integrated transparent electronics (i.e., antennas, sensors, supercapacitors, etc.) and circuits. The high-concentration homogeneous ink forms a conductive film with mirror effect, while a heterogeneous or less uniform  $\text{Ti}_3\text{C}_2\text{T}_x$  ink showing aggregation and oxidation will severely diminish the specular effect or even disappear.

### 4. Experimental Section

**Purification and Size Selection of  $\text{Ti}_3\text{AlC}_2$  MAX Phase:** The as-received MAX phase from Jilin 11 technology Co., Ltd. (10 g, 200 mesh) was stirred vigorously in  $9 \text{ M HCl}$  ( $\approx 30 \text{ mL}$ ) for 12 h at room temperature, then washed several times with deionized water until neutral. Then the

small-sized MAX phase based on Stokes' law according was removed to Equation 6.

$$v = \frac{2(\rho_p - \rho_f)gR^2}{9\mu} \quad (6)$$

where  $g$  is the gravitational acceleration ( $\text{m s}^{-2}$ ),  $R$  is the particle sizes,  $\rho_p$  is the mass density of the  $\text{Ti}_3\text{AlC}_2$  particles ( $\approx 4.2 \times 10^3 \text{ kg m}^{-3}$ ),  $\rho_f$  is the mass density of water ( $\text{kg m}^{-3}$ ), and  $\mu$  is the dynamic viscosity ( $\text{Pa s}$  or  $\text{kg m}^{-1} \text{ s}^{-1}$ ) of water ( $8.90 \times 10^{-4} \text{ Pa s}$  at  $\approx 25 \text{ }^\circ\text{C}$ ). The large-sized MAX phase was obtained following a modified version of the previously reported method.<sup>[32]</sup> Specifically, the purified MAX phase was dispersed in a centrifuge tube filled with deionized water (height =  $10 \text{ cm}$ ) and shaken evenly by hand, and then left for 8.5 min to rapidly remove the upper suspension and precipitate into MAX phase larger than  $10 \mu\text{m}$ . The settlement process was performed 3 times.

**Synthesis of Delaminated  $\text{Ti}_3\text{C}_2\text{T}_x$ :** The delaminated  $\text{Ti}_3\text{C}_2\text{T}_x$  was obtained by using the classical etching method. LiF (1.6 g) was completely dissolved in  $9 \text{ M HCl}$  solution (20 mL), following 1 g MAX phase was added to the solution for 36 h at  $45 \text{ }^\circ\text{C}$  under stirring. Subsequently, the precipitate was washed until the pH  $\approx 6$ , and then the sediment was dispersed and centrifuged repeatedly 3–5 times for sufficient intercalation and delamination. Further, the sample was continuously shaken by vortex oscillator for 30 min to improve the yield, and the delaminated  $\text{Ti}_3\text{C}_2\text{T}_x$  was obtained by centrifugation at 1500 rcf for 30 min. Finally, the upper suspension was centrifuged at 3000 rcf for 30 min (3 times) to remove the small-sized  $\text{Ti}_3\text{C}_2\text{T}_x$  flakes. Finally, the delaminated  $\text{Ti}_3\text{C}_2\text{T}_x$  was diluted to a specific concentration for slot-die coating.

**Production of Transparent and Conductive Thin-Films:** The TCEs films were fabricated by slot-die coating on diverse substrates in a class 5 clean-room. First, glass substrates were cleaned with a soap solution, ethanol, deionized water, sequentially. Before slot-die coating, all substrates were plasma cleaned (Diener Plasma surface technology) for 2 min under vacuum ( $0.47 \text{ mbar}$ ) to obtain a hydrophilic surface. The TCEs were prepared with various transparency by adjusting the concentration of  $\text{Ti}_3\text{C}_2\text{T}_x$  solution (key-factor) and the gap height. Specifically, such as,  $\text{Ti}_3\text{C}_2\text{T}_x$  dispersion  $< 3 \text{ mg mL}^{-1}$  for  $T > 80\%$ ,  $0.5\text{--}1 \text{ mg mL}^{-1}$  for  $T > 90\%$ ,  $3\text{--}8 \text{ mg mL}^{-1}$  for  $60\% < T < 80\%$  at gap height  $\approx 38 \mu\text{m}$ . The opaque films were fabricated from  $\approx 30 \text{ mg mL}^{-1}$   $\text{Ti}_3\text{C}_2\text{T}_x$  ink (without removing the small-sized  $\text{Ti}_3\text{C}_2\text{T}_x$  flakes) at gap height  $\approx 250 \mu\text{m}$ . The substrate stage moving rate was controlled at  $0.5 \text{ m min}^{-1}$  ( $0.3\text{--}1 \text{ m min}^{-1}$ ). The flow rate of the solution was controlled at  $0.5 \text{ mL min}^{-1}$  ( $0.3\text{--}1 \text{ mL min}^{-1}$ ). The transparent and opaque films were transferred to the glove box (Ar atmosphere) and annealed at the relevant temperature (glass and PI substrates at  $180 \text{ }^\circ\text{C}$  for 4 h, PET and PDMS substrates at  $110 \text{ }^\circ\text{C}$  for 2 h) to remove the interlayers water between the flakes, after natural cooling for later use.

**Morphology Characterization:** SEM and TEM characterization of the samples were carried out on a NanoSEM 230 and JEOL 2200 FS (200 kV), respectively. XRD measurements were performed on X'Pert Pro with Cu  $K_\alpha$  radiation ( $\lambda = 0.15406 \text{ nm}$ ). AFM characterization and analysis of samples were performed on a Bruker ICON3 in the peak force scan-asyst mode and NanoScope analysis software 2.0, respectively. Raman spectra of  $\text{Ti}_3\text{C}_2\text{T}_x$  films were collected on a Renishaw Raman microscope (633 nm). GISAXS of all films was measured using a Bruker NanoStar (Bruker AXS GmbH, Karlsruhe, Germany). Herman's orientation factor ( $f$ ) was calculated according to the Equations 7 and 8,<sup>[32,45]</sup> which represents the degree of orientation of the  $\text{Ti}_3\text{C}_2\text{T}_x$  flakes with respect to the glass substrate.

$$f = \frac{3 \cdot (\cos^2\varnothing)}{2} \quad (7)$$

where  $(\cos^2\varnothing)$  is the mean-square cosine calculated from the scattered intensity  $I(\varnothing)$  integrated over the azimuthal angle following:



$$(\cos^2\varphi) = \frac{\int_0^{\pi/2} I(\varphi) \cdot \sin\varphi \cdot \cos^2\varphi \cdot d\varphi}{\int_0^{\pi/2} I(\varphi) \cdot \sin\varphi \cdot d\varphi} \quad (8)$$

The Herman's orientation factor ( $f$ ) values from  $-0.5 \leq f \leq 1.0$ . If  $f$  was equal to  $-0.5$ , orientation was perpendicular to the reference, that is, flow, direction ( $\varphi = 90^\circ$ ). If  $f$  was equal to 1, the scattering structure was parallel to the reference direction ( $\varphi = 0^\circ$ ), and if  $f$  was equal to 0, a random orientation was present. Orientation direction was established based on the peak maxima on the azimuthal profile and established to be parallel to the substrate ( $\varphi = 0^\circ$ ).

**Optoelectronic Performance Measurements:** The transmittance measurements of the  $\text{Ti}_3\text{C}_2\text{T}_x$  TCEs were performed on a UV-vis spectrophotometer (Varian Cary 50) in the wavelength range 350–800 nm. The transmittance at 550 nm was defined as the transmittance of the  $\text{Ti}_3\text{C}_2\text{T}_x$  TCEs from average of 5 different areas. The sheet resistance ( $R_s$ ) was tested with a four-point probe (Jandel, Model RM3-AR), the values were obtained by averaging 10 different regions for each sample. The thickness of all samples was measured using a programable surface profiler (DEKTA 6 m), and defined as the average values from 5 different areas. A  $\text{Ti}_3\text{C}_2\text{T}_x$  thin film sample on glass was characterized with variable angle spectroscopic ellipsometry in the wavelength range 370–1690 nm using an M-2000VI instrument (J.A. Woollam Co., Inc., Lincoln, NE 68 508 USA). Measurements were performed using incidence angles of  $50^\circ$ ,  $60^\circ$ , and  $70^\circ$ , where  $0^\circ$  corresponds to perpendicular incidence. A B-spline fit respecting the Kramers–Kronig relation was applied to extract both the layer thickness ( $200 \pm 5$  nm) and the optical constants.

**Electrochemical Characterization:** Preparation of PVA/ $\text{H}_2\text{SO}_4$  gel electrolyte: First, 1 g of polyvinyl alcohol (PVA,  $M_n = 72\,000$ ) powder was dissolved in 10 mL of deionized water at  $80\text{--}90^\circ\text{C}$  under stirring, until the solution became clear. Subsequently, after cooling to room temperature, 1.64 mL of concentrated  $\text{H}_2\text{SO}_4$  (97 wt.%) was slowly added to the above solution under ice bath and stirring, and the evenly mixed gel electrolyte was kept in dark place.  $\text{Ti}_3\text{C}_2\text{T}_x$  films with different thicknesses were patterned to obtain MSCs by laser scribing (TruMark Station 5000, Trumpf). The patterns of interdigital-type microsupercapacitors were designed by TRUMPF software (finger gap  $\approx 260$   $\mu\text{m}$ ). The CV, GCD, and cycling ability were measured using a VMP3 potentiostat (BioLogic, France). The area specific capacitance of all microsupercapacitors was calculated from the 4th cycle of each CV tests by Equation 9,

$$C = \frac{\int_0^{0.6} j dV}{A \Delta V \nu} \quad (9)$$

where,  $C$  is the area specific capacitance of MSC,  $j$  is the current (mA),  $\Delta V$  is the safe voltage window (0.6 V),  $A$  is the geometric area of the MSC (0.38  $\text{cm}^2$ ), and  $\nu$  is the scan rate ( $\text{mV s}^{-1}$ ). The area specific capacitance of the MSC was also calculated through the 4th cycle of each GCD curve according to Equation 10,

$$C/A = \frac{j \cdot t}{A \cdot \Delta V} \quad (10)$$

where  $\Delta V$  is the effective voltage window excluding the IR drop and  $\Delta t$  is the discharge time.

## Supporting Information

Supporting Information is available from the Wiley Online Library or from the author.

## Acknowledgements

C.Z. and J.H. designed the project and experiments. T.G. performed materials synthesis and characterization experiments and wrote the original manuscript. D.Z. commented on the manuscript and supported the research of T.G. C.Z. and J.H. detailedly commented on the manuscript several times. S.D., M.G., J.W., and J.H. helped with the partial characterization experiments for this manuscript. M.J. provided the film's Raman and TEM measurements. E.H. provided the film's spectroscopic ellipsometry characterization and analysis. J.A. and A.N. provided the film's GISAXS characterization and analysis. All the authors reviewed and commented on the manuscript. The work was supported by the Fundamental Research Funds for the Central University, the 111 Project of China (B14040) from Xi'an Jiaotong University, and China Scholarship Council (202106280247). This research was generously supported by "the Fundamental Research Funds for the Central Universities (1082204112A26)". C.F.Z. thanks the National Natural Science Foundation of China (22209118). Funding from the ETH board (SFA-AM project SCALAR) is acknowledged.

Open access funding provided by ETH-Bereich Forschungsanstalten.

## Conflict of Interest

The authors declare no conflict of interest.

## Data Availability Statement

The data that support the findings of this study are available from the corresponding author upon reasonable request.

## Keywords

MXenes, percolation, slot-die coating, transparent conductive electrodes

Received: November 12, 2022

Revised: January 5, 2023

Published online: February 7, 2023

- [1] S. Bai, X. Guo, X. Zhang, X. Zhao, H. Yang, *Compos. Part A: Appl. Sci.* **2021**, *149*, 106545.
- [2] H. W. Liu, H. L. Tian, C. Du, T. T. Huang, Z. Y. Zhao, D. Zhou, *Adv. Eng. Mater.* **2021**, *23*, 2100115.
- [3] S. K. Sharma, C. D. Sarris, *IEEE J. Flex. Electron.* **2022**, *1*, 174.
- [4] a) C. K. Jeong, D. Y. Hyeon, G. T. Hwang, G. J. Lee, M. K. Lee, J. J. Park, K. I. Park, *J. Mater. Chem. A* **2019**, *7*, 25481; b) Y. Liu, L. Wang, Y. Mi, S. Zhao, S. Qi, M. Sun, B. Peng, Q. Xu, Y. Niu, Y. Zhou, *J. Mater. Chem. C* **2022**, *10*, 13351.
- [5] a) D. S. Hecht, L. Hu, G. Irvin, *Adv. Mater.* **2011**, *23*, 1482; b) Z. Li, H. Li, X. Zhu, Z. Peng, G. Zhang, J. Yang, F. Wang, Y. F. Zhang, L. Sun, R. Wang, J. Zhang, Z. Yang, H. Yi, H. Lan, *Adv. Sci.* **2022**, *9*, 2105331.
- [6] C. Zhang, V. Nicolosi, *Energy Storage Mater.* **2019**, *16*, 102.
- [7] S. De, T. M. Higgins, P. E. Lyons, E. M. Doherty, P. N. Nirmalraj, W. J. Blau, J. J. Boland, J. N. Coleman, *ACS Nano* **2009**, *3*, 1767.
- [8] S. De, J. N. Coleman, *ACS Nano* **2010**, *4*, 2713.
- [9] S. Lu, J. Shao, K. Ma, D. Chen, X. Wang, L. Zhang, Q. Meng, J. Ma, *Carbon* **2018**, *136*, 387.
- [10] N. Kim, S. Kee, S. H. Lee, B. H. Lee, Y. H. Kahng, Y. R. Jo, B. J. Kim, K. Lee, *Adv. Mater.* **2014**, *26*, 2268.
- [11] A. Shayesteh Zeraati, S. A. Mirkhani, P. Sun, M. Naguib, P. V. Braun, U. Sundararaj, *Nanoscale* **2021**, *13*, 3572.

- [12] M. Hossain, K. P. Sabin, K. D. M. Rao, *J. Mater. Chem. C* **2021**, *9*, 6257.
- [13] S. Kang, T. Kim, S. Cho, Y. Lee, A. Choe, B. Walker, S. J. Ko, J. Y. Kim, H. Ko, *Nano Lett.* **2015**, *15*, 7933.
- [14] a) W. Chen, L. X. Liu, H. B. Zhang, Z. Z. Yu, *ACS Nano* **2020**, *14*, 16643; b) P. Wang, C. Zhang, M. Wu, J. Zhang, X. Ling, L. Yang, *Nanomaterials* **2021**, *11*, 1360.
- [15] a) A. VahidMohammadi, J. Rosen, Y. Gogotsi, *Science* **2021**, *372*, 1165; b) S. J. Wan, X. Li, Y. Chen, N. N. Liu, Y. Du, S. X. Dou, L. Jiang, Q. F. Cheng, *Science* **2021**, *374*, 96.
- [16] C. J. Zhang, L. McKeon, M. P. Kremer, S. H. Park, O. Ronan, A. Seral-Ascaso, S. Barwich, C. O. Coileain, N. McEvoy, H. C. Nerl, B. Anasori, J. N. Coleman, Y. Gogotsi, V. Nicolosi, *Nat. Commun.* **2019**, *10*, 1795.
- [17] a) T. Guo, M. Fu, D. Zhou, L. Pang, J. Su, H. Lin, X. Yao, A. S. B. Sombra, *Small Struct.* **2021**, *2*, 2100015; b) T. Guo, D. Zhou, L. Pang, M. A. Darwish, Z. Shi, *Scripta Mater* **2022**, *213*, 114590.
- [18] G. Ma, H. Shao, J. Xu, Y. Liu, Q. Huang, P. L. Taberna, P. Simon, Z. Lin, *Nat. Commun.* **2021**, *12*, 5085.
- [19] a) Z. Zeng, C. Wang, G. Siqueira, D. Han, A. Huch, S. Abdolhosseinzadeh, J. Heier, F. Nuesch, C. J. Zhang, G. Nystrom, *Adv. Sci.* **2020**, *7*, 2000979; b) X. Wu, T. Tu, Y. Dai, P. Tang, Y. Zhang, Z. Deng, L. Li, H. B. Zhang, Z. Z. Yu, *Nano-Micro Lett.* **2021**, *13*, 148.
- [20] X. Xu, Y. Chen, P. He, S. Wang, K. Ling, L. Liu, P. Lei, X. Huang, H. Zhao, J. Cao, J. Yang, *Nano Res.* **2021**, *14*, 2875.
- [21] K. Hantanasirisakul, T. Chantaurai, A. Limsukhon, P. Chomkhuntod, P. Poprom, M. Sawangphruk, *Adv. Mater. Interfaces* **2022**, *9*, 2201457.
- [22] a) P. Salles, E. Quain, N. Kurra, A. Sarycheva, Y. Gogotsi, *Small* **2018**, *14*, 1802864; b) A. D. Dillon, M. J. Ghidui, A. L. Krick, J. Griggs, S. J. May, Y. Gogotsi, M. W. Barsoum, A. T. Fafarman, *Adv. Funct. Mater.* **2016**, *26*, 4162; c) D. Wen, X. Wang, L. Liu, C. Hu, C. Sun, Y. Wu, Y. Zhao, J. Zhang, X. Liu, G. Ying, *ACS Appl. Mater. Interfaces* **2021**, *13*, 17766.
- [23] a) C. J. Zhang, B. Anasori, A. Seral-Ascaso, S. H. Park, N. McEvoy, A. Shmeliov, G. S. Duesberg, J. N. Coleman, Y. Gogotsi, V. Nicolosi, *ACS Appl. Mater. Interfaces* **2015**, *7*, 16495.
- [24] K. Hantanasirisakul, M. Q. Zhao, P. Urbankowski, J. Halim, B. Anasori, S. Kota, C. E. Ren, M. W. Barsoum, Y. Gogotsi, *Adv. Electron. Mater.* **2016**, *2*, 1600050.
- [25] P. Salles, D. Pinto, K. Hantanasirisakul, K. Maleski, C. E. Shuck, Y. Gogotsi, *Adv. Funct. Mater.* **2019**, *29*, 1809223.
- [26] J. H. Kim, G. S. Park, Y. J. Kim, E. Choi, J. Kang, O. Kwon, S. J. Kim, J. H. Cho, D. W. Kim, *ACS Nano* **2021**, *15*, 8860.
- [27] a) M. S. Carvalho, H. S. Kheshgi, *AIChE J.* **2000**, *46*, 1907; b) B. G. Higgins, L. E. Scriven, *Chem. Eng. Sci.* **1980**, *35*, 673.
- [28] R. B. Rebouças, I. R. Siqueira, M. S. Carvalho, *J. Non-Newton. Fluid* **2018**, *258*, 22.
- [29] I. R. Siqueira, R. B. Rebouças, M. S. Carvalho, *AIChE J.* **2017**, *63*, 3187.
- [30] a) C. J. Zhang, M. P. Kremer, A. Seral-Ascaso, S. H. Park, N. McEvoy, B. Anasori, Y. Gogotsi, V. Nicolosi, *Adv. Funct. Mater.* **2018**, *28*, 1705506; b) C. J. Zhang, S. H. Park, A. Seral-Ascaso, S. Barwich, N. McEvoy, C. S. Boland, J. N. Coleman, Y. Gogotsi, V. Nicolosi, *Nat. Commun.* **2019**, *10*, 849.
- [31] K. Hantanasirisakul, M. Alhabeb, A. Lipatov, K. Maleski, B. Anasori, P. Salles, C. Ieasakurat, P. Pakawatpanurut, A. Sinitskii, S. J. May, Y. Gogotsi, *Chem. Mater.* **2019**, *31*, 2941.
- [32] J. Zhang, N. Kong, S. Uzun, A. Levitt, S. Seyedin, P. A. Lynch, S. Qin, M. Han, W. Yang, J. Liu, X. Wang, Y. Gogotsi, J. M. Razal, *Adv. Mater.* **2020**, *32*, 2001093.
- [33] A. D. Rakic, A. B. Djuricic, J. M. Elazar, M. L. Majewski, *Appl. Opt.* **1998**, *37*, 5271.
- [34] a) W. Chen, X. Gui, L. Yang, H. Zhu, Z. Tang, *Nanoscale Horiz.* **2019**, *4*, 291; b) L. Yang, T. Niu, H. Zhang, W. Xu, M. Zou, L. Xu, G. Cao, A. Cao, *2D Mater.* **2017**, *4*, 041001.
- [35] H. Shao, K. Xu, Y. C. Wu, A. Iadecola, L. Liu, H. Ma, L. Qu, E. Raymundo-Piñero, J. Zhu, Z. Lin, P. L. Taberna, P. Simon, *ACS Energy Lett.* **2020**, *5*, 2873.
- [36] a) T. Bashir, S. A. Ismail, J. Wang, W. Zhu, J. Zhao, L. Gao, *J. Energy Chem.* **2023**, *76*, 90; b) A. Sarycheva, M. Shanmugasundaram, A. Krayev, Y. Gogotsi, *ACS Nano* **2022**, *16*, 6858.
- [37] a) J. Tang, T. S. Mathis, N. Kurra, A. Sarycheva, X. Xiao, M. N. Hedhili, Q. Jiang, H. N. Alshareef, B. M. Xu, F. Pan, Y. Gogotsi, *Angew. Chem., Int. Ed.* **2019**, *58*, 17849; b) J. Halim, K. M. Cook, M. Naguib, P. Eklund, Y. Gogotsi, J. Rosen, M. W. Barsoum, *Appl. Surf. Sci.* **2016**, *362*, 406.
- [38] C. J. Zhang, S. Pinilla, N. McEvoy, C. P. Cullen, B. Anasori, E. Long, S. H. Park, A. Seral-Ascaso, A. Shmeliov, D. Krishnan, C. Morant, X. Liu, G. S. Duesberg, Y. Gogotsi, V. Nicolosi, *Chem. Mater.* **2017**, *29*, 4848.
- [39] S. Kumar, D. Kang, V. H. Nguyen, N. Nasir, H. Hong, M. Kim, D. C. Nguyen, Y. J. Lee, N. Lee, Y. Seo, *ACS Appl. Mater. Interfaces* **2021**, *13*, 40976.
- [40] Y. Liang, J. Frisch, L. Zhi, H. Norouzi-Arasi, X. Feng, J. P. Rabe, N. Koch, K. Mullen, *Nanotechnology* **2009**, *20*, 434007.
- [41] X. Wang, L. Zhi, K. Müllen, *Nano Lett.* **2008**, *8*, 323.
- [42] Y. Gao, Y. S. Zhou, W. Xiong, L. J. Jiang, M. Mahjouri-samani, P. Thirugnanam, X. Huang, M. M. Wang, L. Jiang, Y. F. Lu, A. P. L. Mater, **2013**, *1*, 012101.
- [43] T. Chen, Y. H. Xue, A. K. Roy, L. M. Dai, *ACS Nano* **2014**, *8*, 1039.
- [44] Y. Y. Peng, B. Akuzum, N. Kurra, M. Q. Zhao, M. Alhabeb, B. Anasori, E. C. Kumbur, H. N. Alshareef, M. D. Ger, Y. Gogotsi, *Energy Environ. Sci.* **2016**, *9*, 2847.
- [45] M. Vangurp, *Colloid. Polym. Sci.* **1995**, *273*, 607.